DENTAL MATERIALS 35 (2019) 1576–1593

Available online at www.sciencedirect.com

ScienceDirect

journal homepage: www.intl.elsevierhealth.com/journals/dema

Investigations into the interface failure of yttria partially stabilised zirconia - porcelain dental prostheses through microscale residual stress and phase quantification

Alexander Lunt[a,*], *Enrico Salvati*[b], *Nikolaos Baimpas*[b,1], *Igor Dolbnya*[c], *Tee Khin Neo*[d], *Alexander M. Korsunsky*[b]

[a] *Department of Mechanical Engineering, University of Bath, Bath, BA2 7AY, UK*
[b] *Department of Engineering Science, University of Oxford, Oxford, OX1 3PJ, UK*
[c] *Diamond Light Source, Harwell Science and Innovation Campus, Didcot, OX11 0QX, UK*
[d] *Specialist Dental Group, Mount Elizabeth Orchard, #08-03/08-08/08-10, 228510, Singapore*

ARTICLE INFO

Keywords:
Micro-focus X-ray diffraction
Raman spectroscopy
Yttria partially stabilised zirconia-porcelain dental prostheses
Residual stress analysis
Phase mapping

ABSTRACT

Objectives. Yttria Partially Stabilised Zirconia (YPSZ) is a high strength ceramic which has become widely used in porcelain veneered dental copings due to its exceptional toughness. Within these components the residual stress and crystallographic phase of YPSZ close to the interface are highly influential in the primary failure mode; near interface porcelain chipping. In order to improve present understanding of this behaviour, characterisation of these parameters is needed at an improved spatial resolution.

Methods. In this study transmission micro-focus X-ray Diffraction, Raman spectroscopy, and focused ion beam milling residual stress analysis techniques have, for the first time, been used to quantify and cross-validate the microscale spatial variation of phase and residual stress of YPSZ in a prosthesis cross-section.

Results. The results of all techniques were found to be comparable and complementary. Monoclinic YPSZ was observed within the first 10 μm of the YPSZ-porcelain interface with a maximum volume fraction of 60%. Tensile stresses were observed within the first 150 μm of the interface with a maximum value of ≈ 300 MPa at 50 μm from the interface. The remainder of the coping was in mild compression at ≈ −30 MPa, with shear stresses of a similar magnitude also being induced by the YPSZ phase transformation.

Significance. The analysis indicates that the interaction between phase transformation, residual stress and porcelain creep at YPSZ-porcelain interface results in a localised porcelain fracture toughness reduction. This explains the increased propensity of failure at this location, and can be used as a basis for improving prosthesis design.

Abbreviations: DIC, digital image correlation; FIB, focused ion beam; FIST, full in-plane strain tensor; MBLEM, Multi Beam Laboratory for Engineering Microscopy; SEM, scanning electron microscopy; TEM, transmission electron microscopy; XRD, X-ray diffraction; YPSZ, yttria partially stabilised zirconia.

[*] *Corresponding author.*
E-mail address: a.j.g.lunt@bath.ac.uk (A. Lunt).

[1] Present address: Atkins Ltd, London Rd, Derby DE24 8UP, UK.

https://doi.org/10.1016/j.dental.2019.08.098

1. Introduction

Yttria Partially Stabilised Zirconia (YPSZ) is a high strength, biocompatible, phase-transforming ceramic which has become widely used in the manufacture of dental prostheses due to its high fracture toughness [1,2]. YPSZ derives its resistance to crack propagation from the stress-induced tetragonal to monoclinic phase transformation [3]. The tensile stress field at crack tips are sufficient to induce the transformation that is associated with a 7% volumetric expansion. This expansion acts to close the crack tip, thereby increasing the energy required to propagate the crack and leading to an increased toughness [4].

In dental applications, YPSZ does not possess the aesthetic pearlescence of enamel and has a hardness which is sufficient induce wear of patients existing teeth during occlusion [5]. YPSZ dental prosthesis are therefore incrementally veneered with multiple layers of porcelain in order to build up the shape of the prosthesis and to tailor the surface finish. Unfortunately this manufacturing approach is associated with the primary failure mode of YPSZ-porcelain dental prosthesis; near interface chipping of the porcelain veneer [6,7].

The origins of this near-interface failure are not fully understood, however the build-up of residual stress at the interface has been proposed as one potential explanation [8,9]. These stresses are induced by the coefficient of thermal expansion mismatch between the YPSZ and porcelain, the tetragonal to monoclinic transformation in YPSZ and tempering of the near-interface porcelain [10]. Several micromechanical techniques have previously been applied in order to study the residual stress state within YPSZ copings. Fardin et al. used nanoindentation to determine the average residual stress across the YPSZ porcelain interface at a resolution of 10 μm [11], Sebastiani et al. applied the ring-core Focused Ion Beam (FIB) milling and Digital Image Correlation (DIC) technique to determine the average residual stress at a few points of interest [12], and Inokoshi et al. revealed large variations in average residual stress within a few microns of the interface using Raman spectroscopy [13].

The underlying relationships that exist between phase, microstructure and mechanical properties in YPSZ mean that isolated examination of the residual stress is insufficient to understand fully the nature of the near-interface failure. Recent studies have revealed distinct variations in fracture toughness, yield strength and Young's modulus within the near-interface YPSZ, at the locations where high magnitude stresses have previously been reported [14,15]. Evidence for the tetragonal to monoclinic phase transformation at YPSZ-porcelain interface has also been recently presented using Raman spectroscopy and Transmission Electron Microscopy (TEM) [13,14]. This transformation has been shown to be influenced by the veneering approach, in particular whether dry or wet porcelain is used [16,17]. It is also known that the application of surface manipulations such as sawing, fracturing, or sandblasting are sufficient to induce a highly localised (microscale) transformations at YPSZ edges [18].

Despite these observations, the literature contains numerous studies that have been unable to observe this behaviour in clinically representative samples [19,21]. One potential explanation for these differing results is the resolution with which previous characterisation has been performed. Therefore, there is an arising need for a comprehensive assessment of the microscale variation of YPSZ phase composition, residual stress magnitude and principal orientations within YPSZ copings, in order to improve understanding of the interplay between these effects.

The aim of this study is to develop and apply the experimental techniques necessary to investigate the phase and residual stress distribution within a representative YPSZ-porcelain dental prosthesis at the microscale. Cross-validation of these new techniques has been critical to ensure the validity of the results presented and therefore three independent techniques are presented; transmission X-Ray Diffraction (XRD), Raman spectroscopy and FIB microscale-milling. Comparisons between the YPSZ-porcelain interface and the YPSZ free edge of the sample has been performed in order to provide improved insight and validation of the results presented. These insights will help improve understanding of the origins of chipping in these components in order to achieve the long term objective of reducing failure rates after implantation.

2. Materials and methods

2.1. Sample preparation

The incisal dental prosthesis used in this study was selected from a batch of prosthodontic crowns which were produced for the Specialist Dental Group, Singapore. In order to be representative of clinical samples, the manufacturing processes used to create these prostheses were identical to those used in commercial dental restorations. Computer aided manufacture was used to form the YPSZ coping from Wieland Dental Zenotec Zr Bridge [22] which was then sintered to produce a fully dense component. The composition of this material is given in Table 1. The sintering process was performed following the manufacturer's instructions with an initial temperature hold at 900° before being heated to 1500°C. The sample temperature was then reduced to room temperature, with incrementally reduced cooling rates at lower temperatures.

A multi-stage veneering process of Ivoclar Vivadent IPS e.max Ceram was applied to the YPSZ coping in order to build up the desired shape of the completed prosthesis. The average elemental composition of this material is shown in Table 1. The coping was initially ultrasonically cleaned in water for 10 min, no additional staining was applied and the porcelain was applied wet in all cases. The veneering procedure was performed in accordance with the manufacturer's instructions [23] as follows. Firstly, a layer of ZirLiner was applied at 960 °C using a heating rate of 40 °C/min. This step was followed by a wash firing and dentin firing at 650 °C at a heating rate of 90 °C/min. Finally, a glaze was applied to the prosthesis at 710 °C and a heating rate of 60 °C/min.

In order to facilitate access to the YPSZ-porcelain interface, the sample was embedded in a two-part epoxy resin and a Buehler IsoMet® low speed saw was used to obtain a 2 mm thick section of the centre of the prosthesis. A 10 cm diameter blade, rotational speed of 90 rpm and load of 0.75 N was used

Table 1 – Composition of Wieldand Dental Zenotec Zr Bridge YPSZ coping [16] and Ivoclar Vivdaent IPS e.max Ceram porcelain veneer [17] (in weight %).

Oxide	ZrO_2	Y_2O_3	HfO_2	Al_2O_3	SiO_2	Na_2O	K_2O	ZnO	CaO, P_2O_5, F	Other oxides	Pigments
Zenotec Zr Bridge	88–95.5	4.5–6	<5	<0.5	–	–	–	–	–	<0.5	–
IPS e.max Ceram	–	–	–	8–12	60–65	6–9	6–8	2–3	2–6	2–8.5	0.1–1.5

to minimise the residual stresses induced during sectioning. A four stage diamond grit and colloidal silica polishing approach was then applied to each surface in order to minimise the zone affected by sample preparation to a sub-micron (≈ 0.15 μm) region and to thin the sample. A final thickness of 115 μm was selected in order to maximise the transmission of diffracted signal during X-ray diffraction.

In general, porcelain chipping is primarily observed on the occlusal surfaces of YPSZ prostheses, as the thermal gradients at this location are largest during the firing process [24]. This generates the largest magnitude residual stresses and leads to an increased likelihood of failure at this location [25]. This occlusal surfaces also typically respond to the smallest radius of curvature of the YPSZ-porcelain interface and the largest variations in veneer thickness. Therefore, small deviations in measurement position or angle can potentially lead to significant differences in the properties being measured.

In order to minimise this effect, and ensure that the most comparable results were obtained by the independent methods applied in this study, the analysis was instead performed on the side walls of the crown as shown in Fig. 1. At this location the interface has the largest radius of curvature and most uniform veneer thickness. As a result, the influence of positional or angular error in the measurements were minimised. In particular this ensured that the data sets obtained by the FIB milling, which were implicitly associated with an offset along the line of the interface, were as comparable as possible.

2.2. *Experimental methods*

2.2.1. *Micro-focus X-ray diffraction*

Synchrotron micro-focus X-ray diffraction was performed on Beamline B16 at Diamond Light Source, Harwell, UK. In order to minimise sample absorption, a monochromatic 17.9 keV incident beam (just below the 18.0 keV K-edge of Zr) was selected using a double crystal monochromator. A transmission setup similar to that previously successfully implemented by Lunt et al. [26] was used for this study. Samples were mounted onto two crossed Newport 25 mm linear translation stages in order to facilitate 2D translation in a direction perpendicular to the beam at a precision better than ± 0.1 μm. Kirkpatrick–Baez mirrors were used to focus the incident beam to a spot size of 2.8 × 3 μm^2 and a Zeiss Stereo Optical Microscope was used to place the samples in the focal plane. A Photonic Science X-ray Image Star 9000 detector was placed 169 mm downstream of the sample to record 2D cross-sections of the Debye–Sherrer diffraction cones at this position and calibration of this sample to detector distance was performed using Si powder. Radiographs of the samples were captured using a Photonic Science MiniFDI X-ray eye, which were used to align the sample to the focused beam.

In order to generate the smooth, high intensity diffraction peaks necessary for strain quantification, an XRD exposure time of 480 sec at each point was required. Analysis was initially performed at salient points on three different samples to ensure that consistent results were observed. Complete characterisation was then performed on a single sample. A 60 point 2.8 μm incremental line scan was performed on this sample at the YPSZ – porcelain interface at a position 3 mm below the apex of the YPSZ free surface as shown in Fig. 1. A similar 60 point scan was then performed from the free surface of the YPSZ along the same scanning axis.

2.2.2. *Raman spectroscopy*

Raman spectroscopy was performed using the Renishaw inVia Raman confocal microscope at the Research Complex at Harwell, UK. A laser power of 15 mW, excitation frequency of 514 nm and non-polarised objective lens of 100 times was used to capture the required spectra. Taking into account the magnification, incident wavelength and any scattering phenomena, the nominal spot size of this study was expected to be ≈ 1 μm diameter.

In order to prevent sample drift during scanning, the sample was mounted onto a Scanning Electron Microscopy (SEM) stub with silver paint. In order to align the sample to the same position as the XRD study, the apex of the YPSZ free surface was located optically and stage translation was used to offset the sample by 3 mm. An exposure time of 120 sec was required to produce a clear spectrum with low levels of background noise at each point. Two incremental line scans with a 1 μm step were performed on the prosthesis cross-section in order to provide direct comparison with the XRD results as shown in Fig. 1. The first was a 170 point line scan which was performed from the near interface porcelain towards the bulk YPSZ and the second was a 170 point line scan from the free surface of the YPSZ into the bulk.

2.2.3. *FIB milling*

FIB milling for comparative residual stress analysis was performed using the Tescan Lyra 3 FIB-SEM at the Multi Beam Laboratory for Engineering Microscopy (MBLEM), Oxford, UK [27]. In order to reduce the impact of charging during SEM imaging and FIB milling, a 5 nm coat of Au/Pd was sputtered onto the prosthesis cross section. A working distance of 9 mm, SEM beam voltage of 5 keV, FIB beam energy of 30 keV and ion current of 750 pA was used for both the sequential and parallel FIB milling. In order to improve the surface contrast and thereby facilitate improved DIC, a single pass of the FIB was applied to the sample surface prior to milling. This approach generates a stable, random surface pattern (as shown in Fig. 1) which has been shown to aid effective marker tracking while minimising residual stresses induced in the surface [26,28].

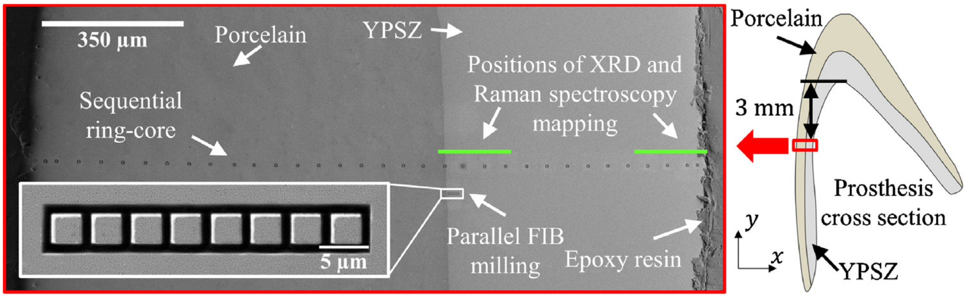

Fig. 1 – Schematic diagram of prosthesis cross section showing approximate location of mapping. The insert shows the relative positions of XRD and Raman spectroscopy mapping regions, as well as that of the sequential and parallel ring-core FIB milling.

Tilt corrected SEM imaging was used in this study using the same approach that has been successfully employed in other investigations [29,30].

The location of the sequential FIB milling was determined by placing the sample in the orientation shown in Fig. 1, locating the apex of YPSZ free surface and then shifting the sample 3 mm. During this analysis sequential ring-core milling was also performed over the porcelain veneer, and the results of this analysis have been published elsewhere [31,32]. The parallel FIB milling approach was then implemented at an offset of 75 μm relative to the sequential analysis as shown in Fig. 1. This distance was selected as a balance between reducing the effect of stress relief induced by previous milling to less than $< 0.2\%$ [28] on the one hand, and measuring residual stress states which were directly comparable, on the other.

2.2.3.1. *Sequential ring-core FIB milling.* The sequential ring-core FIB milling approach is a microscale spatially resolved residual stress analysis technique which can be used to determine absolute in-plane near-surface residual stresses at the lateral spacing of $10 - 1000$ μm [28,33]. This technique is based on incremental FIB milling of the ring-core milling geometry [34–36] with careful consideration of relaxation induced by milling of previous measurement points. The resolution and length scale associated with this method are suitable for stress quantification across the entire prosthesis as shown in Fig. 1.

In this study thirteen 5 μm diameter micro-pillars were milled using a trench width of 1 μm and a nominal distance of 50 μm between stress measurements. This ensured that the influence of previous measurement points on subsequent stress measurements was guaranteed to be <0.5%. A measurement was also made near the free surface of YPSZ at a distance of 25 μm from the nearest point. At this point the previous measurement was guaranteed only to be less than 2%. Incremental FIB milling was performed at each location with a nominal milling depth of 100 nm between the SEM image collection. For each micro-pillar, fifty 2048 × 2048 pixel micrographs were captured using a pixel size of $4.4 \times 4.4\,\text{nm}^2$ in a total time of approximately 35 min.

2.2.3.2. *Parallel FIB milling.* Parallel FIB milling is a new high spatial resolution (micro-scale) residual stress analysis technique which can be used to map stress variation at the lateral spacing of 1–10 μm by simultaneously milling multiple cores [28]. The maximum number of islands that can be milled simultaneously is limited by the maximum pixel dimension with which a single SEM image can be captured (which is typically on the order of ≈10,000–100,000 pixels). High resolution (nanoscale) pixel sizes are required to perform reliable DIC and therefore the length scale over which DIC markers can be analysed is limited to a few 10's of microns. This approach has therefore been developed for localised residual stress analysis [37]. In this study the parallel FIB milling technique has been applied to quantify the residual stresses within a few microns from the YPSZ-porcelain interface, close to the position at which porcelain chipping is known to originate [38].

Eight islands of dimension $3 \times 3\ \mu\text{m}^2$ were milled in this study as shown in Fig. 1. A trench width of 1 μm was used, resulting in a quantitative measurement of residual stress every 4 μm. SEM images of total field of view size of 8192 × 2048 pixels were captured at each milling step using a pixel size of $4.4 \times 4.4\,\text{nm}^2$. A nominal milling depth step of 25 nm was selected to minimise the impact of milled material redeposition on the surface of the islands and the resulting DIC quality degradation. In total, 160 images were collected in approximately 3 h.

2.3. *Analytical techniques*

2.3.1. YPSZ *phase mapping*

XRD and Raman spectroscopy have become well established techniques for monoclinic phase volume fraction analysis of YPSZ [39–42]. In these original calibration studies, tetragonal and monoclinic YPSZ powders were mixed with known volume fractions, from which XRD patterns and Raman spectra were collected. In the case of XRD, the differing crystal plane symmetries of tetragonal and monoclinic YPSZ result in distinct diffraction peaks, and for Raman spectroscopy the differing excitation peaks of tetragonal and monoclinic YPSZ are observed in the spectra of inelastic scattering response, as shown in Fig. 2 [43]. The relative intensities of these peaks, in combination with the empirical relationships derived from experiments, can be used to provide quantitative estimates of the monoclinic volume fraction.

2.3.1.1. *Micro-focus X-ray diffraction phase mapping.* Monoclinic volume fraction analysis of the diffraction data was performed by 360° radial integration of the 2D diffraction pat-

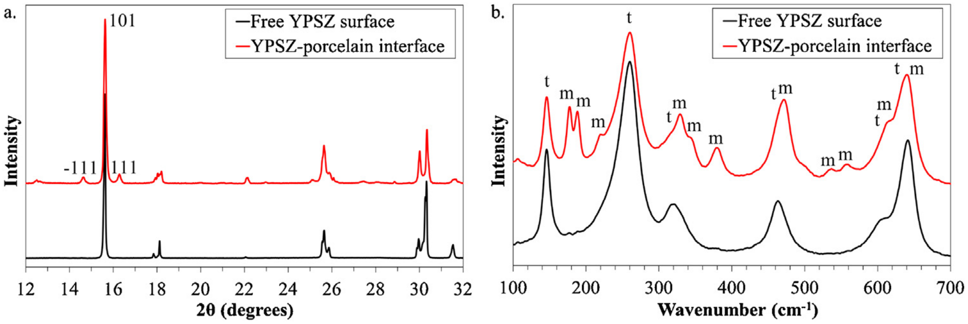

Fig. 2 – (a) XRD intensity against scattering angle for the free YPSZ surface and the YPSZ-porcelain interface. The 101 tetragonal peak and the -111 and 111 monoclinic peaks have been indicated. (b) Wavenumber against intensity obtained by Raman spectroscopy at the free YPSZ surface and the YPSZ-porcelain interface. The monoclinic and tetragonal peaks have been indicated.

terns about the beam centre. This approach reduces all of the scattering data into a single 1D distribution of intensity against scattering angle (2θ), and thereby maximises the precision with which volume fraction can be determined.

The phase intensity ratio in the sample X_m can be determined from the ratios of integrated intensity of the tetragonal 101 $\left(I^t_{101}\right)$, monoclinic -111 $\left(I^m_{-111}\right)$, and monoclinic 111 $\left(I^m_{111}\right)$ diffraction peaks using the expression [3]:

$$X_m = \frac{I^m_{-111} + I^m_{111}}{I^m_{-111} + I^m_{111} + I^t_{101}} \tag{1}$$

X_m can then be used to obtain estimates of the monoclinic volume fraction (V_m) from [39]:

$$V_m = \frac{1.311X_m}{1 + 0.311X_m} \tag{2}$$

In order to provide reliable estimates of the integrated intensity of the diffraction peaks, least square fitting of Gaussian peaks was performed using:

$$f\left(2\theta\right) = \alpha e^{-\frac{(2\theta-\beta)^2}{2s^2}} \tag{3}$$

where α is the peak height, β is the peak centre and s is the peak width parameter. The integrated area beneath these fitted peaks is given by:

$$I = \sqrt{2\pi}\alpha s \tag{4}$$

The main benefit of using the Gaussian peak fitting approach, rather than the simple summation of data points on the curve, is that least squares fitting provides standard deviation estimates of the fitted parameters α and s. These in turn can be used to quantify the standard deviations of X_m, V_m and I. Importantly, this enables the computation of the confidence intervals of the volume fraction estimates.

2.3.1.2. *Raman phase mapping.* In the context of Raman spectroscopy, peak intensity is defined as the number of counts recorded at the peak apex [40]. This is equivalent to peak height (α) in the previous section. Consistent notation has been used in this section to enable cross-comparison.

A number of empirical relationships between monoclinic volume fraction and Raman peak intensity have been proposed in the literature [43,44]. The most widely used empirical relationship to determine monoclinic volume fraction from Raman data was put forward by Clarke & Adar [45]:

$$V_m = \frac{\alpha^m_{178} + \alpha^m_{189}}{0.97\left(\alpha^t_{145} + \alpha^t_{260}\right) + \alpha^m_{178} + \alpha^m_{189}} \tag{5}$$

where α superscripts refers to the tetragonal (t) or monoclinic (m) phase attribution of the peak, and subscripts refer to the wavenumber of the peak centre in cm^{-1}.

The peaks appearing in Raman spectroscopy profiles are known to display a combination of Gaussian and Lorentzian character however a Gaussian distribution is known to give a good approximation for the spectra obtained from the solid materials [46]. In order to provide estimates of peak intensity α, least squares Gaussian peak fitting was performed on the Raman spectra using a modified version of Eq. 3. These values were then used to determine the variation of the monoclinic volume fraction using Eq. 5. The standard deviation value of peak heights were also combined in accordance with Eq. 5 to provide estimates of the 95% confidence intervals of V_m.

2.3.2. *Residual stress analysis*

2.3.2.1. *Tetragonal lattice strain and stress.* In recent decades, strain tensor quantification using powder XRD has become a well-established technique. It exploits the strain-induced changes in the diffraction peak positions to gain insight into lattice strain variation with the azimuthal angle (φ) [9,47,48], that corresponds to the in-plane strain direction. To give precise estimates of the lattice strain, this approach requires sharp, clearly defined diffraction peaks with high signal-to-noise ratios. In the case of YPSZ, the highest intensity peak is associated with the tetragonal phase that corresponds to the reflection from the family of lattice planes with the Miller index 101, as shown in Fig. 2. This property, in combination with the prevalence of tetragonal YPSZ at both the YPSZ-porcelain interface and the YPSZ surface, makes this the optimal choice for in-plane strain tensor analysis in this study.

A comprehensive overview of in-plane strain tensor analysis of YPSZ prostheses has previously been published, and the following analysis is based on this work [26]. Azimuthal integration of the 2D diffraction data was performed over 10° sectors to provide 1D profiles of average intensity against 2θ scattering angle for 36 orientations within the sample plane (normal to the incident beam). For example, the 1D profile for 0° orientation was obtained by integrating from $\varphi = -5°$ to $\varphi = 5°$. Gaussian peak fitting of the form shown in Eq. 3 was next applied to determine the tetragonal 101 peak centre position as a function of azimuthal angle, $\beta^{101}(\varphi)$. Bragg's law can then be used to convert this to estimates of the tetragonal 101 lattice spacing $d^{101}(\varphi)$ which in turn can be used to estimate the tetragonal 101 lattice strain $\varepsilon^{101}(\varphi)$ through:

$$\varepsilon^{101}(\varphi) = \frac{d^{101}(\varphi) - d_0^{101}}{d_0^{101}} \tag{6}$$

The expression d_0^{101} represents the unstrained lattice parameter of the tetragonal 101 peak which has previously been determined to be 2.9586 ± 0.004 [28]. This numerical value is based on the assumption that the through sample average obtained by XRD is best represented by a plane stress state, due to the sample's thinness. The validity of this approximation is discussed in more detail in Section 4.2.

In order to determine the principal strains (ε_1 and ε_2) and principal direction with respect to the laboratory coordinate frame (ϕ), the azimuthal variation of the 101 tetragonal lattice strain was fitted with the strain transformation formula that can be obtained e.g. from Mohr's strain circle:

$$\varepsilon(\varphi) = \frac{\varepsilon_1 + \varepsilon_2}{2} + \frac{\varepsilon_1 - \varepsilon_2}{2}\cos 2(\varphi + \phi) \tag{7}$$

A weighted least square approach was used for fitting, and the standard deviation values of the azimuthal lattice strain estimates were obtained by propagation of the peak centre uncertainties through Bragg's law and Eq. 6. This analysis provided estimates of the standard deviation of ε_1, ε_2 and ϕ.

The magnitudes of the principal in-plane residual stresses (σ_1 and σ_2) were then obtained using Hooke's law for plane stress conditions:

$$\sigma_1 = \frac{E}{1-\nu^2}(\varepsilon_1 + \nu\varepsilon_2) \tag{8}$$

$$\sigma_2 = \frac{E}{1-\nu^2}(\varepsilon_2 + \nu\varepsilon_1) \tag{9}$$

where E is Young's modulus (210 GPa) and ν is Poisson's ratio (0.3) for YPSZ [22,49].

The YPSZ-porcelain interface introduces a key geometric orientation within the system, and therefore the shear (τ) and direct stresses were resolved in directions parallel (σ_{Pa}) and perpendicular (σ_{Pe}) to the interface through the expressions:

$$\sigma_{Pa,Pe} = \frac{\sigma_1 + \sigma_2}{2} \pm \frac{\sigma_1 - \sigma_2}{2}\cos 2\phi \tag{10}$$

$$\tau = \frac{\sigma_1 - \sigma_2}{2}\sin 2\phi \tag{11}$$

Estimates of the confidence intervals of each of these stresses were obtained by propagation of the standard deviations of ε_1, ε_2 and ϕ through Eqs. 8–11).

2.3.2.2. Sequential ring-core FIST analysis. As previously explained, a line array of sequential ring-core FIB milling markers (micro-pillars) was performed across both the YPSZ and porcelain veneer layers within this sample. The results of porcelain residual strain quantification in directions parallel and perpendicular to the YPSZ-porcelain interface have previously been published elsewhere [31,32]. However, for the analysis that follows, insight into the full in-plane strain tensor was necessary. Therefore, the FIST ring-core analytical approach was applied [26]. This analysis was performed on the micro-pillar markers within the YPSZ region, and was also used to reanalyse the data previously collected from the porcelain veneer layer. Although identical steps of analysis were taken for both materials, YPSZ has been selected as the main focus of this study. Therefore the improved insight into the residual stress state in porcelain has been included in the compendium of mechanical microscopy results at the YPSZ-porcelain interface in Section 4.3.

The analysis stages necessary to perform ring-core FIB milling and DIC full strain tensor analysis have recently been described in detail in the literature [26]. This approach is based on determining the angular variation of strain relief in the core by repeated implementation of the strain quantification routine originally pioneered by Korsunsky et al. [34]. This involves the digital positioning of several thousand DIC subset markers at the surface of the milled core (micro-pillar) which are tracked by DIC through the sequence of SEM images collected during milling [50]. At each milling depth the gradient of marker displacement against its position can be used to estimate the uniform strain relief in the core, once care has been taken to remove outliers from the data set at this stage. Several automated routines have been developed to leave only the well tracked markers, as described in a recent review article [29]. In the analysis presented here, correlation coefficient thresholding was performed at 0.5, standard deviation thresholding was performed for markers with this parameter greater than 1.5 times the average, and the removal of outliers to the expected displacement field was performed for offsets greater than 1.5 times the average. These threshold values have previously been found to be effective at removing poorly tracked markers in a diverse array of studies, and were manually checked during each analytical procedure to ensure consistency.

The resulting profiles of strain relief against milling depth (or image number) were then fitted using the finite element relief 'master curve' published by Korsunsky et al. [51] to provide estimates of the average residual strain which was originally present within the core, in a given direction. This analysis was then repeated in order to determine the residual strain variation as a function of angle within the plane of the sample (in increments of 10°). Similar to the XRD analysis, these distributions were fitted with the $\cos(2\varphi)$ variation given in Eq. (7) to determine the principal residual strains and orientations. Hooke's law (Eqs. (8) and (9)) was then used to determine the principal stresses using a plane stress approximation and the supplier's Young's modulus and Poisson's ratios. In order to extract comparable results, these stresses were then resolved in the directions parallel and perpendicular to the interface in order to determine the direct and shear stress components in each case (Eqs. (10) and (11)).

To provide reliable confidence interval estimates for the residual stress and orientation estimates obtained from this analysis, careful error propagation was performed throughout the entire analytical procedure [29]. Weighted least squares fitting was performed using the inverse standard deviation of each data point or variable estimate. Full confidence intervals of each estimate were also propagated through the entire strain to stress conversion process. The only variables taken as absolute measures were Young's modulus and Poisson's ratio for both materials, since no confidence intervals were known for these parameters.

2.3.2.3. *Parallel FIB milling.* Parallel FIB milling analysis was carried out in a region lying 75 μm along the interface relative to the sequential milling area in order to reduce the impact of any relaxation from previous milling, as shown in Fig. 1. The location of milling relative to the YPSZ-porcelain interface was intended to capture the response of the near interface region, where XRD stress analysis was thought to be least reliable.

The close proximity, bloc type milling performed during the parallel FIB milling approach presents challenges to applying full in-plane strain tensor analysis routines [52]. It is also worth noting that the islands, or cores produced no longer possess circular symmetry [53]. Therefore, residual stress analysis was only performed in directions parallel and perpendicular to the YPSZ-porcelain interface during this study. Analysis of each of the cores was performed incrementally by digitally positioning markers and running automated DIC analysis of the sequence of SEM images collected [50]. The same outlier removal parameters were used as those used for the sequential analysis to leave only well-tracked markers in the least squares fitting of strain relief.

The presence of neighbouring markers was found to influence the strain relief against milling depth curves obtained during this analysis in a similar manner that had previously been observed during other studies [28,37]. Clear plateaus were observed in all strain relief distributions, indicating that milling had been performed to a depth sufficient to induce full strain relief, a requirement that has recently been demonstrated and discussed further using eigenstrain analysis [54,55]. Therefore, the approach using the finite element 'master curve' published by Korsunsky [51] was applied.

This analysis was performed on all measurement points in order to obtain residual stress estimates in directions parallel and perpendicular to the interface at each location. The same error quantification and propagation procedures used for the sequential FIB milling were performed during the parallel FIB milling analysis.

2.3.2.4. *Raman Peak shift analysis.* The relationship between Raman peak centre position and residual stress is well-established and has been the focus of several dedicated research articles [40,56]. The generic approach in these studies was to record Raman spectra during the application of known forces, and then to quantify the linear relationship between stress and peak centre [57]. Typically these studies were performed using uniaxial tension or controlled bending, and the maximum principal stress was used in the associated calibration procedure. In the case of YPSZ it has however recently been shown that the trace ($\sigma_{11} + \sigma_{22} + \sigma_{33}$) of the stress tensor demonstrates the strongest correlation with Raman peak centre positions [56]. Consideration of the stress tensor within the near-surface of uniaxial or controlled bending specimens reveals that this stress invariant is in fact well approximated by the maximum principal stress (as the other two principal stresses can be considered to be $\approx$ 0MPa). Therefore, the calibration procedures performed in these studies are still valid, provided that the first stress invariant is used as the input, and not simply the maximum principal stress value.

The relationships between peak centre position and the sum of the three principal stress values can therefore be used as method of validating the stress estimates obtained from the tetragonal lattice 101 reflection analysis. Importantly, this approach is independent of the crystal orientation and is representative of the average behaviour within the entire family of tetragonal grains. The absence of monoclinic peaks in the majority of the spectra prevented reliable stress quantification from being performed in this phase.

In order to determine the most suitable peaks for peak centre analysis, the distribution of peaks in Fig. 2b was used. Five distinct peaks can be observed within the tetragonal spectrum corresponding to wavenumbers of 145 cm^{-1}, 260 cm^{-1}, 318 cm^{-1}, 461 cm^{-1}, and $\approx$630 cm^{-1}. This latter peak is a convolution of three peaks at 605 cm^{-1}, 635 cm^{-1} and 641 cm^{-1} which were found to have different peak shift responses under the application of stress [40]. This presents difficulties for reliable peak fitting, and therefore the peak cluster around $\approx$ 630 cm^{-1} was not analysed further. The former four peaks were found to yield effective measures of peak centre shift under stress within bulk YPSZ. However, the presence of monoclinic phase in the near-interface region resulted in peak overlap and led to difficulties in reliable peak fitting for the 318 cm^{-1} and 461 cm^{-1} tetragonal peaks (due to the 304 cm^{-1} and 479 cm^{-1} monoclinic peaks, respectively). Gaussian peak fitting was therefore performed only for the tetragonal peaks at 145 cm^{-1} and 260 cm^{-1} to obtain estimates of the peak centre and the associated confidence interval at each position.

In order to provide approximate estimates of the first stress invariant, the in-plane principal stresses obtained by XRD at each location were added together. This approach intrinsically assumes that within the Raman spectroscopy gauge volume, the out of plane stress component is much smaller than the in-plane stresses. Linear interpolation was next applied to the sum of the principal XRD stress values in order to derive estimates of this value at each Raman measurement location (since XRD and Raman spectroscopy were performed at different distinct points).

3. Results

3.1. *Phase distribution*

The distribution V_m of at both the YPSZ-porcelain interface and the YPSZ free surface are shown as a function of distance from the sample edge in Fig. 3. The results obtained from XRD and Raman spectroscopy show very similar trends over the

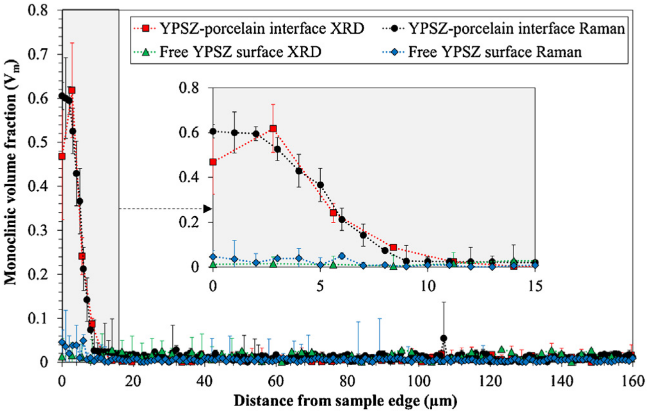

Fig. 3 – Monoclinic volume fraction as a function of distance from the YPSZ-porcelain interface and YPSZ free edge. The results of both XRD and Raman spectroscopy analysis are shown, along with the 95% confidence intervals of each data point. Graph inset shows region 0–15 µm from the edge in more detail.

entire 160 µm characterised region. An inset of the first 15 µm has been included to provide enhanced detail at the location where the steepest variation and maximum V_m values are present. At this location, edge effects lead to a reduction in signal intensity, which is demonstrated by larger confidence intervals. For this reason, the precise error bound propagation that has been performed during this study has been essential for reliable data interpretation.

3.2. *Residual stress analysis*

The residual stress distributions within the YPSZ obtained through XRD and FIB milling are shown as a function of distance from the YPSZ-porcelain interface in Fig. 4. As previously discussed, XRD analysis was only performed close to the interface region and at the free edge. The sequential FIB milling results were obtained across the entire cross section, and parallel FIB milling was performed close to the YPSZ-porcelain interface. Figs. 4a and 4b show the direct stress variation in directions parallel and perpendicular to the interface, respectively. It should be noted that the XRD and sequential FIB milling results were able to capture the full in-plane stress tensor and the corresponding shear stress and the angular offset between the principal stress direction and the interface orientation (ϕ) have been also been plotted in Fig. 4c and d, respectively.

The sequential FIB milling residual stress estimate obtained at the YPSZ-porcelain interface was obtained from a bi-material core. This resulted in additional experimental difficulties, and the average Young's modulus and Poisson's ratio (of YPSZ and porcelain) was used in the strain to stress calculation for this data point. Although the results of this analysis appear to have provided realistic estimates of stress, large uncertainty intervals are associated with these values. In order to prevent similar issues during the parallel milling, this data collection routine was offset by 3 µm from the interface.

3.3. *Raman spectroscopy*

The relationship between peak centre position and XRD first stress invariant was found to be approximately linear for both the 145 cm^{-1} and 260 cm^{-1} peaks, as shown in Fig. 5. Total least squares fitting was applied to determine the gradient (Π) and axis intercept (ω) of this distribution. For the 145 cm^{-1} peak this was determined to be $\Pi = -0.58 \pm 0.01\ \text{cm}^{-1}/\text{GPa}$ and $\omega = 145.28 \pm 0.01\ \text{cm}^{-1}$, and for the 260 cm^{-1} peak, $\Pi = -1.19 \pm 0.02\ \text{cm}^{-1}/\text{GPa}$ and $\omega = 259.98 \pm 0.01\ \text{cm}^{-1}$.

4. Discussion

4.1. *Monoclinic YPSZ phase distribution*

The results of XRD phase mapping near the YPSZ-porcelain interface reveals a high concentration ($\approx 40-60\%$) of monoclinic YPSZ within the first 2.8 µm of the interface. At further distances from the interface, the monoclinic volume fraction reduces until purely tetragonal YPSZ is observed at distances greater than ~11 µm.

Within this study, the position of the YPSZ-porcelain interface was defined by the first diffraction pattern in which the YPSZ XRD peaks could be reliably fitted. Some evidence for very weak diffraction peaks was observed in the porcelain diffraction pattern collected at a nominal position of −2.8 µm from the interface, indicating that the precision of this alignment is only to within the increment between measurement points. Further, some low intensity porcelain diffraction was observed in the near interface diffraction patterns which reduced the peak fitting precision and resulted in increased 95% confidence intervals for the first 2 points.

It is important to note that the XRD monoclinic volume analysis of the YPSZ free surface detected no evidence of tetragonal to monoclinic phase transformation at this location. The transition from epoxy to YPSZ was more distinct than that observed at the YPSZ-porcelain interface (with a single increment between no YPSZ diffraction and clear peaks), indicating that this interface was either sharper or more closely aligned to the incident beam.

Raman spectroscopy phase analysis of the YPSZ-porcelain interface demonstrates a monoclinic volume fraction distribution which is very similar to the results obtained through XRD. Three points with approximately 60% monoclinic phase were observed within the first 3 µm of the interface which was followed by a monoclinic volume fraction reduction over the next 7 µm towards a purely tetragonal phase state.

At both the YPSZ free edge, and at distances beyond 10µm from the YPSZ-porcelain interface, no clear evidence for monoclinic YPSZ was obtained in the Raman spectroscopy study. This matches the results of the XRD analysis. Moreover, similar minor variations in the monoclinic volume fraction were observed. The largest discrepancy is observed in an outlier at 108 µm from the interface, which upon closer examination has no monoclinic peaks present but relatively large amounts of noise at 178 cm^{-1} and 189 cm^{-1}.

The results obtained within this study demonstrate that a high volume fraction of monoclinic YPSZ is present within the first 2.8µm of the interface. This correlates well with TEM

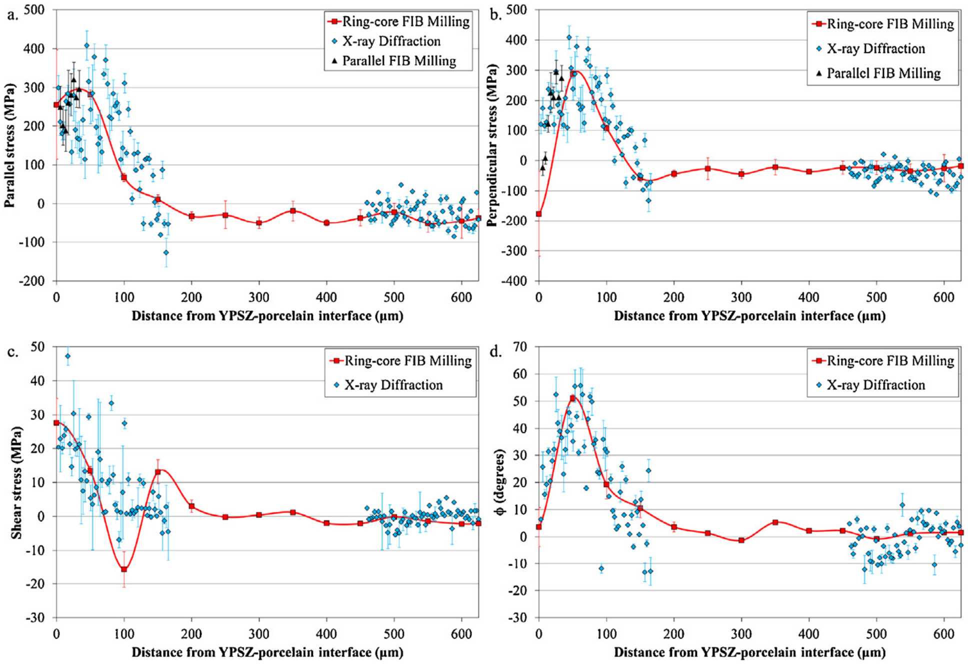

Fig. 4 – Residual stresses resolved into the coordinate system aligned with the YPSZ-porcelain interface as a function of distance from this position. The free YPSZ edge of the sample is located at ≈625 μm from the interface. The results obtained from X-ray diffraction, ring-core FIB milling and parallel milling are included in plots of direct stress in directions (a) parallel and (b) perpendicular to the interface, as well as (c) the associated shear stresses and (d) the angular offset ϕ from the principal coordinates. The 95% confidence intervals of each measurement are indicated by the error bars.

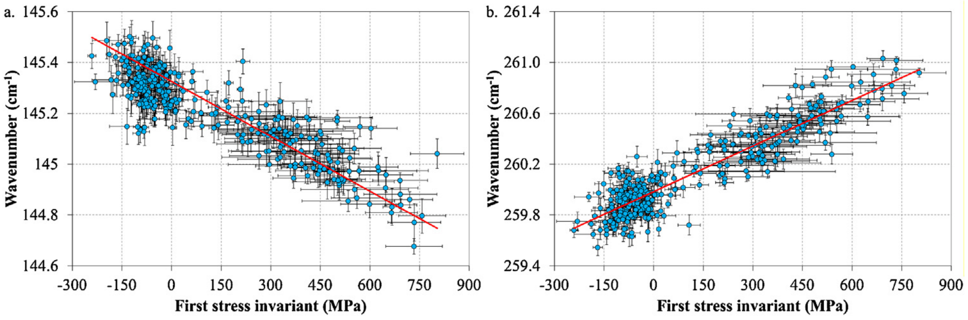

Fig. 5 – Raman peak centre vs interpolated XRD first stress invariant for the tetragonal Raman peaks with nominal peak centres of (a) 145 cm^{-1} and (b) 260 cm^{-1}. The 95% confidence intervals of each data point are indicated by the error bars and the results of total linear least squares fitting are shown.

analysis of the YPSZ-porcelain interface [14] in which a similar sized region of twinned YPSZ was observed. The tetragonal to monoclinic phase transformation is known to induce shear through micro-scale twinning [58,59] and TEM studies of interfaces within YPSZ solid oxide fuel cells have shown very similar features at locations where the tetragonal to monoclinic phase transformation is induced [60,61]. This highly localised transformation is characteristic of a boundary level effect which is similar to those observed at other interfaces within the literature [62,63]. Predicting the length scales over which two materials interact at an interface is known to be particularly challenging, and work is ongoing in order to better encapsulate these effects in analytical or finite element simulations.

Examination of the literature reveals that the tetragonal to monoclinic phase transformation has been previously been observed at the YPSZ-porcelain interface of specially manufactured test samples in which the YPSZ had been sandblasted prior to the application of the porcelain veneer [13,42]. Several studies have also identified monoclinic YPSZ at the zirconia-porcelain interface in representative samples [13,16] however the maximum monoclinic volume fraction estimates that were obtained in these studies were lower than the values identified in the present analysis (11.5% and 30%, respectively). It should be noted that these volume fraction estimates are necessarily an average of a grain by grain phenomena, in that any given grain is either monoclinic or tetragonal. This average is dependent on the number of grains in a given phase, their sizes and the gauge volume that has been characterised by a given technique. Therefore, one potential explanation for the differences between the results of our study and those previously presented in the literature is the size and shape of the gauge volume implemented. Given the larger gauge volumes cross sectional sizes ($50 \times 200\ \mu m^2$ and $10 \times 10\ \mu m^2$, respectively) used in these studies [13,16], it is perhaps unsurprising that these results differ to those presented in the present study.

The absence of monoclinic YPSZ at the free surface of YPSZ indicates that porcelain is necessary to induce the phase transformation. The driving force for this phase change could therefore be potentially associated with several factors:

1. Elemental composition exerts a strong influence on the transformability of YPSZ [64,65]. Diffusion across the interface between porcelain and YPSZ could provide a basis for explaining the transformation observed. However, recent energy dispersive spectroscopic analysis of these types of YPSZ-porcelain interface has demonstrated maximal diffusional distances of less than 3 μm into the YPSZ region [14]. Therefore, the 10 μm width of transformed region cannot be fully explained by this effect.
2. The presence of water is known to result in the low temperature degradation of YPSZ from a tetragonal to monoclinic phase [66,67]. It is therefore possible that the presence of wet porcelain may induce a similar localised transformation effect. This is particularly likely during the sintering process, as increased temperatures are known to increase the rate of degradation, particularly in the range of 200 – 300 °C [68].
3. Thermal history is also known to play a critical role in the phase transformation of YPSZ [69]. The sintering process associated with the application of porcelain veneer to the YPSZ-porcelain interface creates different thermal history at the YPSZ free surface and in the near-interface location. However, despite these differences, this explanation is insufficient to explain why the phase transformation is only induced within a narrow band at the YPSZ-porcelain interface and does not extend further into the YPSZ bulk (where the thermal history is almost identical).
4. The tetragonal to monoclinic phase transformation is known to be induced by both applied and residual stresses [43,70,71]. The complex residual stress state induced at the YPSZ-porcelain interface is the most likely origin of the phase transformation observed [72,73]. The tensile stresses found at this location [72] may be sufficient to drive the system towards the monoclinic phase. This response has previously been observed in microscale near-interface regions of surfaces of dental YPSZ in which tensile stresses have been induced by fracture or cutting [18,74].

4.2. *Residual stress analysis*

4.2.1. *XRD residual stress variation*

Within this study, XRD estimates of the in-plane residual stress state have been determined from the YPSZ lattice strain calculated on the basis of tetragonal 101 peak. This measure of strain is representative of a subset of the polycrystalline material, and therefore validation of the stress distributions using the independent FIB milling techniques was crucial to ensure confident interpretation.

In transmission XRD experiment a through-thickness sample volume is illuminated, and therefore an average is obtained over both the near surface regions (close to plane stress conditions) and bulk (well approximated by plane strain). Refinement of the unstrained 101 lattice parameter of YPSZ has recently been performed in order to facilitate direct comparison between the results of FIB milling and XRD analysis, and this parameter has been used in this study [26].

The in-plane variation of residual strain was found to correspond well with the $\cos(2\varphi)$ dependence for almost all data points collected. In a few locations, high noise levels resulted in low quality fitting, as indicated by the large 95% confidence intervals at these points.

Examination of the stress and orientation distributions (Fig. 4) reveals that the residual stress estimates obtained through XRD match closely the results of FIB milling, both in terms of magnitude and distribution. The scatter associated with the XRD measurements is far larger than that observed in the FIB milling approach. This variation may be associated with the underlying noise within the diffraction patterns, and its impact on the peak centre quantification.

Examination of the underlying trends in the near-interface XRD analysis reveals high tensile stresses in the order of $\approx 150 - 300$ MPa within the first $\approx 100\ \mu m$ of the interface. A decreasing trend is then observed towards a moderately compressive stress (≈ -50 MPa) at a distance of $\approx 150\ \mu m$ from the interface. In the perpendicular direction a response similar to the parallel direction is observed, with the exception that within the first $\approx 30\ \mu m$ from the interface there is a reduction of stress to between 100 MPa and 200 MPa. The shear variation within this region shows a maximum of approximately 30 MPa at the boundary between YPSZ and porcelain which decreases linearly to a constant near zero stress at distances $\gtrsim 70\ \mu m$ from the interface. The variation in the principal orientation angle, ϕ, indicates that at the near interface location and at approximately 150 μm from the interface, close alignment is observed between principal directions and the interface normals. Between these two points there is a peak in the principal orientation rotation angle with the maximum value of $\approx 50°$ at a distance of $\approx 50\ \mu m$ from the interface.

The XRD residual stress analysis of the free surface shows no clear variation in the parallel, perpendicular or shear stress response. Low magnitude compressive stresses were observed in both the parallel direction (≈ -35MPa) and perpendicular direction (≈ -25 MPa), and the shear stress average value was found to be close to zero. In terms of angular orientation, the principal coordinate system was closely aligned with the YPSZ free edge with minor scatter about this direction.

4.2.2. *Ring-core sequential FIB milling*

Comparison between the results of the ring-core FIB milling and the XRD residual stress analysis reveals similar values both in terms of magnitude and distribution. The $\cos(2\varphi)$ fitting performed as part of the FIST analysis was successful, and tight confidence intervals were observed at all data points except for the marker milled at the YPSZ-porcelain interface. This measurement point also has the largest difference between the results of XRD and the ring-core milling approach; with estimates of ≈ 100MPa and ≈ -180 MPa in a direction parallel to the interface, respectively. These differences may be indicative of the different stress states in the monoclinic and tetragonal phases at this location. Alternatively, it may have arisen due to the bi-material composition of the milled island, and the associated errors in the ring-core measurement. For example, the FIB milling rates of YPSZ and porcelain are known to differ, which resulted in a non-uniform trench depth around the central core. This effect, combined with the differences in mechanical properties and the stress states within the two materials induced relief that is likely to be poorly represented by the homogenous, single value strain tensor analysis outlined above.

At 50 μm from the interface tensile stresses of $\approx 290-300$ MPa were observed in directions parallel and perpendicular to the interface. In both directions a decreasing trend was then observed towards a compressive stress of ≈ -30 MPa at a distance of ~ 200 μm from the interface. Purely compressive stresses were observed at distances beyond 200 μm with average values of ≈ -35 MPa and ≈ -25 MPa for the parallel and perpendicular directions, respectively. The smallest magnitude residual stress was found at the YPSZ free surface in a direction perpendicular to the interface, as expected from the boundary conditions at this location.

The shear stress variation obtained by ring-core milling shows a maximum value of 28 MPa at the YPSZ-porcelain interface. Variations in the shear stress are then observed at the next three points with a magnitude of ±14 MPa. Low magnitude shear stresses are observed across the rest of the porcelain within the range of ±3 MPa.

A variation in the principal angle offset, ϕ, was also observed in the ring-core analysis. The largest angular offsets were 50°, 20° and 10° at the positions 50 μm, 100 μm and 150 μm from the interface, respectively. The remainder of the measurements showed good orientational alignment with the YPSZ-porcelain interface direction with a typical scatter of $\pm 2^\circ$.

4.2.3. *Parallel FIB milling*

The parallel FIB milling residual stress analysis technique was used to provide comparative analysis with the XRD results at the location where monoclinic volume fraction was largest, and the least agreement was found with the results obtained through the sequential ring-core milling approach. During residual stress quantification, the implicit assumption was made that principal axes were aligned with the YPSZ-porcelain interface, i.e. $\phi \approx 0^\circ$. Examination of the distribution of ϕ reveals that, while this is a good approximation for the near-interface region, this approximation is not valid at larger distances. Inaccuracy in this approximation would lead to an error in the stress estimate of the order of shear stress at this location($\approx \pm 20$ MPa). This potential error must therefore be taken into consideration when discussing the results of this analysis.

The magnitude and variation of residual stress determined using the parallel FIB milling approach are generally comparable to the results of XRD and sequential ring-core milling. In the direction parallel to the interface, stresses of magnitude $180-320$ MPa were observed, broadly correlating well with the magnitude of neighbouring stress estimates. Similarly, at distances greater than 13.5 μm from the interface, tensile stresses increasing from $120-320$ MPa are observed which closely match the results of XRD analysis.

The main discrepancy between the parallel ring-core approach and the XRD analysis is observed in a direction perpendicular to the interface at the two measurement points closest to the interface (5.5 μm and 9.5 μm). At this location the XRD residual stress estimate is ≈ 100 MPa, whereas the results of parallel FIB milling indicate a nearly stress-free state. This location corresponds closely to the discrepancy observed between the XRD analysis and sequential ring-core milling analysis (at the YPSZ-porcelain interface), and is the location where the greatest amount of tetragonal to monoclinic phase transformation is observed (Section 4.1). XRD results are representative of the stress state within the tetragonal YPSZ, whereas the FIB milling residual stress analysis provides a measure of the *overall* average stress across both the monoclinic and tetragonal phases (weighted according to the volume fraction of each phase). The difference in the stress estimates obtained using the two techniques suggests that the monoclinic and tetragonal phases may therefore find themselves in different states of residual stress. Similar behaviour has recently been observed using Raman spectroscopy of YPSZ [13]. The exact distribution of stresses and the interaction between these grain groups remain unclear, but the magnitude of stresses may indicate that the volume expansion associated with the tetragonal to monoclinic transformation has relieved the tensile stresses in these grains. This is consistent with the strain energy relaxation in the thermodynamic constructs used to describe this phase transformation response [3].

4.2.4. *Raman spectroscopy stress tensor analysis*

Raman spectroscopy analysis performed in this study was based on unpolarised incident radiation, with no directional sensitivity in terms of residual stress. A representative measure of stress available is the first invariant of the stress tensor (trace). In order to provide representative estimates of this stress measure, interpolation of the XRD results has been performed. Examination of Fig. 5 reveals that this approach, in combination with the high levels of noise in the XRD data results in relatively high levels of uncertainty in the first stress invariant estimates. However, despite these relatively large errors, the large number of data points sampled in this study (particularly with the values of the first invariant in the range $0-150$ MPa) is sufficient to reveal the underlying trend within the data set.

The total least squares fitting performed on this data set reveals a similar response to that previously published by Pezzotti et al. [40], as shown in Table 2. The fitted peak centres at $145.28 \pm 0.01\text{cm}^{-1}$ and $259.98 \pm 0.01\text{cm}^{-1}$ show a reasonable match to the literature values of $144.68\ \text{cm}^{-1}$ and 259.57cm^{-1}, respectively. Raman peak centres are known to be highly sensitive to variations in the elemental composition and thermal processing conditions in YPSZ [75]. The most likely explanation for the minor differences in the peak centre trends are therefore associated with the differences in the chemical makeup and thermal history of the YPSZ examined in this study.

The plots of peak shifts vs first stress invariant were found to have gradients (Π) equal to $-0.58 \pm 0.01\text{cm}^{-1}/\text{GPa}$ and $1.19 \pm 0.02\text{cm}^{-1}/\text{GPa}$ for the peaks with the nominal centres $145\ \text{cm}^{-1}$ and 260cm^{-1}, respectively. This corresponds well

Table 2 – Axis intercept (ω), gradient (Π) and correlation coefficient (R^2) of the relationship between Raman peak centre and first stress invariant for the tetragonal Raman peaks at nominal peak centres of $145\,\text{cm}^{-1}$ and $260\,\text{cm}^{-1}$. Independent literature values obtained by Pezzotti et al. [40] have been included for comparison.

Source	ω (cm^{-1})	Π $(\text{cm}^{-1}/\text{GPa})$	R^2
This study	145.28 ± 0.01	-0.58 ± 0.01	0.77
	259.98 ± 0.01	1.19 ± 0.02	0.84
Pezzotti et al. [27]	144.68	−0.6	0.95
	259.57	1.1	0.76

to the literature values of $-0.6\,\text{cm}^{-1}/\text{GPa}$ and $1.1\,\text{cm}^{-1}/\text{GPa}$ [40]. The minor differences in Π may be indicative of the different elemental compositions and thermal histories of the two types of YPSZ or alternatively may indicate that the first invariant stress values obtained from the 101 tetragonal lattice strain may not be fully representative of the average stress within the tetragonal phase. The large amount of noise within the data set prevents any firm conclusions from being drawn on this suggestion.

Overall the Raman spectroscopy peak centre strain invariant analysis shows good agreement with the values previously published in the literature. This indicates that, despite the large amount of scatter, the results of the XRD 101 tetragonal lattice strain analysis are most likely to be a reasonable estimate of the average stress within the tetragonal regions.

4.2.5. *Residual stress analysis overview*

In this study, the variation of residual stress within the cross section of YPSZ dental coping has been evaluated using XRD, FIB milling and Raman spectroscopy. Overall, the following consistent picture emerges. Tensile stresses are present within the first 100 μm from the YPSZ-porcelain interface with a peak value of ≈ 300 MPa at a distance of 50 μm from the interface. These moderate tensile stresses, in combination with the discrepancies observed between the tetragonal and monoclinic stress state, indicate that stress relief may have been induced by the near-interface phase transformation. The distribution of shear stress within the coping demonstrates a maximum value of ≈ 30 MPa at the YPSZ-porcelain interface which is likely to be associated with the twinning induced at this location by the introduction of the monoclinic phase. Moderate compressive stresses ≈ 30 MPa are observed over the remainder of the prosthesis which are most likely associated with stress equilibration. The principal stress orientations are predominantly parallel to the YPSZ-porcelain boundary close to the interface and the bulk of the YPSZ, with reorientation of up to ≈ 50° being observed at the location of maximum tensile stress and shearing. Further explanation of the potential origins of this residual stress distribution based on the combination with microstructural, micro-mechanical and phase analysis of this region is presented in Section 4.3.

A large number of studies have been performed to simulate and measure the residual stress state within dental veneering media such as porcelain [76–79]. However, comparatively little has been reported on the stress state within YPSZ. A number of similarities between this small selection of studies and the results presented here can be observed: the near-constant compressive stresses across the bulk of the YPSZ coping has previously been observed by Zhang et al. [80] with the magnitude of this stress plateau being shown to be dependent upon both the cooling rate and veneer thickness of the prosthesis [81]. Similar large variations between tensile and compressive stress within the first few microns of the YPSZ-porcelain interface have also been identified by Inokoshi et al. [13].

4.3. *Compendium of mechanical microscopy of the YPSZ-porcelain interface*

In order to improve understanding of the underlying processes responsible for the near-interface residual stresses and phase transformations identified in this study, consideration of the mechanical properties and microstructure at this location is necessary. In this regard, Fig. 6 has been produced as a compendium of the results of high resolution property profiling across the YPSZ-porcelain interface. This Figure includes the results obtained experimentally in this study, but is also the only location within the present article in which previously presented data has been replotted and reinterpreted.

The variation of residual stress across the entire YPSZ-porcelain interface has been determined using FIST sequential ring core residual stress analysis and is shown in Fig. 6a. These results include those presented in Fig. 4, as well as those obtained from the re-evaluation of ring-core FIB milling data previously reported by Lunt et al. [31,32]. Microscale mechanical testing of the YPSZ-porcelain interface has recently been performed to determine the spatial variation of fracture toughness through micropillar splitting [15], as well as the Young's modulus and yield strength from micropillar compression [14] (Fig. 6b). The results of recent energy dispersive spectroscopy studies have also been included to provide insight into the elemental variation in the near-interface region (Fig. 6c) [14]. It can be seen that the elemental composition of both YPSZ and porcelain tend towards the nominal bulk estimates provided in Table 1 at distances greater than 5 μm from the interface.

The variations in phase composition, in combination with these mechanical property studies and the results of recent TEM across the YPSZ-porcelain interface [14] provide a comprehensive overview of the near-interface YPSZ. Within the first 200 nm of the interface a band of small (5 − 70 nm diameter) YPSZ grains are observed. Immediately adjacent to this band lies a region that is ~2 μm -thick region which shows no obvious grain boundaries, but the presence of the high contrast features similar to those observed in monoclinic YPSZ [60,61]. This location and thickness correspond closely with the region containing up to 60% YPSZ monoclinic phase identified within the first 3 μm of the interface using Raman spectroscopy and XRD. The total thickness of the transformed region was ≈ 10 μm, agreeing closely with the12 μm length scale over which increased fracture toughness (by ≈ 10%) was observed within the YPSZ. The larger grain size features and increased monoclinic volume fraction at this location are known to affect fracture toughness through the material propensity to transform [82]. A distinct variation in Young's modulus is also observed within the first 10 μm of the interface, with a reduced stiffness found in four measurements closest to the interface. Monoclinic YPSZ is known to have a

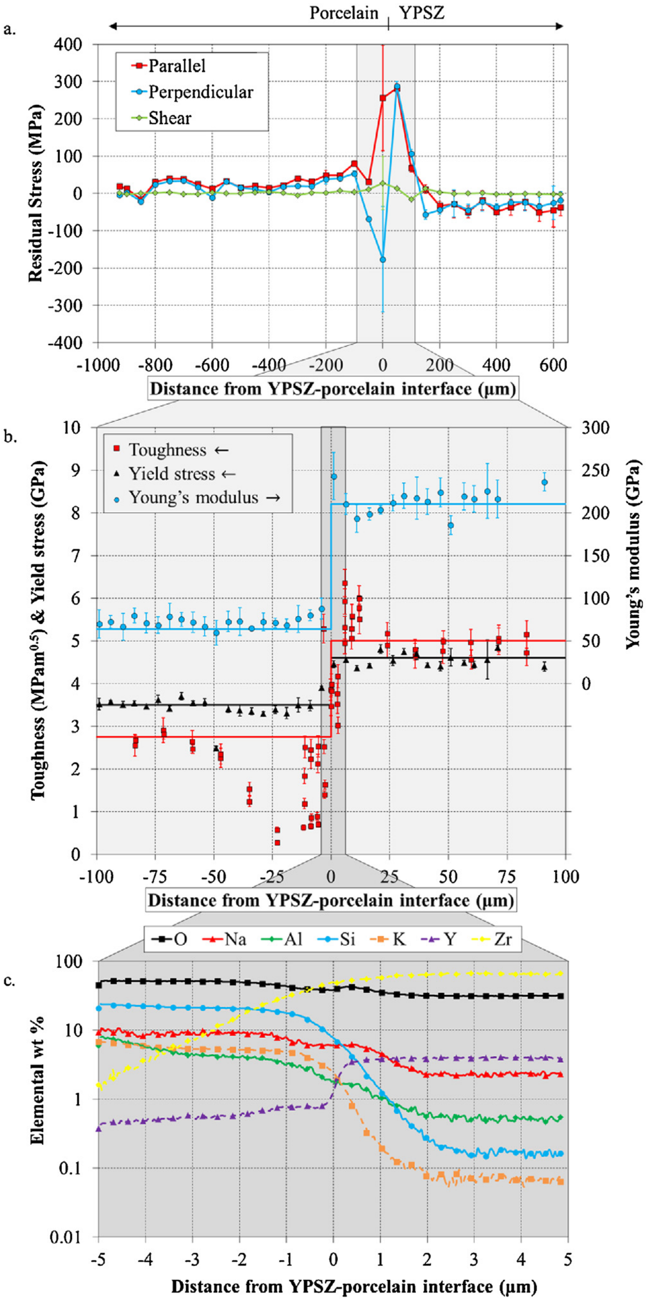

Fig. 6 – Compendium of property profiling across the YPSZ-porcelain interface for residual stress, mechanical properties and elemental composition. Error bars indicate the 95% confidence intervals of each point and where relevant bulk averages are indicated by solid lines. (a) FIST sequential ring-core FIB milling analysis performed across the entire porcelain and YPSZ prosthesis cross-section. Stresses have been resolved in directions parallel and perpendicular to the interface and the results obtained from re-analysing FIB milling presented elsewhere have also been included [31,32]. (b) Microscale variation of fracture toughness, Young's modulus and yield strength from micropillar analysis [14,15]. (c) Spatial variation of seven highest weight % elements obtained using energy dispersive spectroscopy [14].

smaller bulk elastic modulus than tetragonal YPSZ, and this may be the origin of this behaviour [49]. The impact of elemental diffusion may also be influencing the near-interface YPSZ state and mechanical response, with diffusion of silicon being observed up to $2-3\,\mu$m into the YPSZ.

The near-interface porcelain also has characteristic structural features that have consistently been observed using the different analytical techniques applied. Nanoscale voids with the average diameter ~10 nm were observed at distances in the range $0.4-1.5\,\mu$m from the interface [14]. Nanovoiding of this type and size have recently been shown to be induced by high temperature tensile creep at temperatures and stresses similar to those present at the YPSZ-porcelain interface during manufacture [83,84]. Although no nanoscale structural evidence for creep was identified at distances >1.5 µm from the interface, the larger distances over which tensile residual stresses are observed (50–100 µm) indicate that creep may also occur within this region (Fig. 6a). Further evidence for this behavioural response is given by the large (up to ≈ 90%) decrease in the fracture toughness of porcelain within the first 50 µm of the interface (Fig. 6b). Tensile creep damage of similar silica based ceramics have been shown to influence both the fracture toughness and yield strength of these materials [85] and a smaller reduction in yield strength (of up to ≈ 10%) is also observed within the first $10-50\,\mu$m of the interface. Elemental diffusion may also be influencing the mechanical response of the very near-interface region, with the depth of diffusion of zirconium into porcelain found to be ≈ 5 µm. The increased stiffness and yield strength of zirconia may explain the minor increase in these two parameters at the measurement point at 4 µm from the interface.

The conventional design approach which is used in the manufacture of YPSZ-porcelain dental prosthesis is to ensure that the coefficient of thermal expansion of porcelain is moderately lower than that of YPSZ, thereby generating a low magnitude compressive residual stress in the veneer and exploiting the higher magnitude compressive strength of this material (relative to the tensile behaviour) [86]. Despite using this design principle in this study, the average residual stress state within the porcelain has been found to be mildly tensile. This agrees with the results of similar studies within the literature [8,73,80] and suggests that the phase transformation at the YPSZ-porcelain interface is influencing the residual stress in the veneer.

At distances far from the interface, the compressive stresses observed within the YPSZ are likely to be associated with force equilibrium across the coping. The variations in stress state within the porcelain are however most likely associated with the multi-layer coating procedure used to manufacture the veneer [80,84].

4.4. *Mechanistic interpretation of the results*

The combination of microstructural, micromechanical and residual stress analysis obtained in this study provides improved insight into the clinical performance of YPSZ copings. By combining this new information with existing knowledge, potential interpretations for the underlying mechanisms begin to emerge. This section outlines one mechanistic interpretation that explains many of the features observed in this study, and then critically compares this with related YPSZ-porcelain coping characteristics that have previously been identified in the literature.

During manufacture, the porcelain slurry is initially applied to the already sintered YPSZ coping at room temperature. The coping with porcelain paste on its surface is then heated to 750 °C in a vacuum furnace to fire the veneer [87]. During cooling the coefficient of thermal expansion mismatch between the YPSZ and porcelain drives the boundary layer of near-interface porcelain into compression, and the near-interface YPSZ into tension. Strain compatibility and stress equilibrium requires that the thickness of these boundary layers is related to the magnitude of the induced residual stress, and the ratio of Young's moduli of the two materials. In the case of the YPSZ, a region $\approx 150\,\mu\text{m}$ wide appears to be influenced by this process, with the peak stresses located at the YPSZ-porcelain interface.

During cooling, the peak tensile stresses at this near-interface location reach a sufficient magnitude to induce the tetragonal to monoclinic phase transformation in YPSZ [86]. This is associated with a 7% volume expansion in the monoclinic grains and reduces greatly the average tensile stress within this region of YPSZ. Importantly, the relaxation of the neighbouring tetragonal grains may not be as large as that of their monoclinic counterparts. This explains the discrepancy observed between the XRD (exclusively tetragonal phase) and ring-core (overall average) stress evaluation results at this location. The phase change would also induce shear stresses observed at the near-interface location. The observed 60% volume fraction of transformed material within YPSZ leads to expansion strain of up to 4%, which is more than sufficient to replace compressive stresses within the near-interface porcelain veneer with residual tension. It is this locked-in residual stress state at the YPSZ-porcelain interface that acts as the driving force for the porcelain chipping failure.

The next stage of veneer fabrication involves the application of another layer of slurry and reheating the system to 750°C in order to sinter the new material [88]. This temperature is insufficient to melt the proceeding layer of porcelain, but has been shown to be sufficient to induce creep at tensile stresses greater than 100 MPa [83,84]. Tensile creep is activated within the porcelain in the first 50 μm from the interface. This process reduces the residual tensile stresses within this region, but leads to a reduction of fracture toughness and yield stress at the YPSZ-porcelain interface. The application of further veneering layers leads to further mitigation of tensile stresses in the near-interface region, but at the expense of degrading the mechanical integrity of porcelain in this area.

The interaction outlined above provides an explanation for several observations of the YPSZ-porcelain system that have been reported previously. Firstly, the primary failure mode of these prostheses (through porcelain chipping) originates almost entirely from the very near-interface region [89,90]. This is the location of porcelain creep, moderate tensile stresses and the region of greatly reduced mechanical strength. Secondly, thicker veneers are known to result in higher failure rates in YPSZ prostheses [91]. Force equilibrium of the coefficient of thermal expansion mismatch of thicker veneers will result in larger tensile stresses at the YPSZ-porcelain interface, increasing the amount of transformed YPSZ and thereby inducing more damage in the near-interface porcelain. Thirdly, heat treatment of the prosthesis may lead to either increased or reduced integrity, depending upon the conditions and number of cycles applied [92]. This behaviour arises as a consequence of interplay between tensile stress relaxation of the near-interface region and the increased creep damage associated with this process. An optimum thermal cycle may exist that would minimise the induced residual stresses without excessive reduction in mechanical properties. Fourthly, abrasive surface treatment of the YPSZ surface can lead to increased reliability of the prosthesis [93]. Sand or air blasting of the YPSZ surface is known to induce the YPSZ tetragonal to monoclinic phase change within a micro-scale near-interface region [13]. This approach reduces the extent of any further transformation during the sintering cycle, thereby minimising tensile residual stress build up and creep effects in the porcelain veneer. Finally, smaller differences in thermal expansion mismatch lead to increased prosthesis reliability [94]. By reducing the strain mismatch induced between the YPSZ and porcelain during cooling, this approach minimises residual stress build up and creep induced damage in the near-interface porcelain.

Although the mechanistic interpretation outlined above provides a potential explanation for the phase and strain distributions observed in this study, along with several results presented in the literature, it is important to highlight that this analysis has been performed on a single type of YPSZ-porcelain prosthesis. Given the diverse array of manufacturing techniques and methodologies that have been established for the production of YPSZ prostheses, contradictory results and distributions will inevitably be present within the literature. These discrepancies have been covered at depth within several review articles [1,2,20,21,24] however, it is hoped that the insights provided in this study can also begin to provide an explanation for some of these differing results. For example, the importance of porcelain cooling rate on chipping has been widely investigated in the last decade. Many studies have observed that reduced cooling rates can minimise the generation of residual stress at the interface, which reduces failure rates [81,91]. However, in other cases the cooling rate has been shown to have a limited effect on the generation of residual stress and the shear strength of YPSZ-porcelain interfaces [8,95]. The results presented in this study reveal how highly localised variations in phase, residual stress, microstructure, mechanical properties and elemental composition can interact and influence the likelihood of failure in these components. This highlights a potential route for exploring the origins of the discrepancies within the literature, which is critically required in the design and production of reliable prosthesis.

5. Conclusions

In this study, high resolution spatially resolved volume fraction analysis of the constituent phases in dental zirconia was performed using XRD and Raman spectroscopy at the YPSZ-porcelain interface, and at the YPSZ free surface of an all ceramic zirconia-porcelain prosthesis cross section. These independent results were found to be in good agreement, indicating that monoclinic YPSZ is present within the first 10 µm from the interface, with a maximum volume fraction of 60% reached at the YPSZ-porcelain boundary.

Spatially resolved residual stress analysis was performed across the YPSZ cross section in directions parallel and perpendicular to the YPSZ-porcelain interface through the sequential ring core FIB milling and DIC technique, in addition to XRD and Raman spectroscopy. This revealed that the shear-based tetragonal to monoclinic phase transformation at the interface had induced localised shear (≈ 30 MPa) and tensile stresses (≈ 300 MPa). Moderate compressive stresses were observed in the remainder of the coping that have arisen due to stress equilibrium.

Higher resolution residual stress analysis was performed using the parallel FIB milling and DIC technique at the YPSZ-porcelain interface. This indicated that the average residual stress in these two phases is near zero at this location, suggesting that the monoclinic phase is in a differing stress state to the tetragonal YPSZ.

These insights provide a potential explanation for the high near-interface porcelain chipping rates observed, through the following mechanism:

1 The thermal expansion mismatch between YPSZ and porcelain generates high magnitude tensile stresses in the near-interface YPSZ.
2 This induces to the tetragonal to monoclinic phase change at this location.
3 The volume expansion associated with the phase change drives the near-interface porcelain into tension.
4 Further porcelain sintering promotes creep in this region that leads to a reduced mechanical strength.

This interaction provides an explanation for several important observations of the YPSZ interface which have been previously been reported, and enhances existing understanding of how different processing routes can influence prosthesis reliability. The results of this study can therefore be used as a firm basis to optimise models of YPSZ-porcelain prosthesis manufacture, and ultimately aid in reducing failure rates in future.

Acknowledgements

The European Project EU FP7 project iStress (604,646) is acknowledged for the funding support provided to MBLEM, where the FIB milling was carried out. We acknowledge the Research Complex at Harwell and the Centre for In situ Processing Studies for support and the provision of access to Renshaw inVia Raman confocal microscope, and Diamond Light Source for access to beamline B16 (proposal MT8823-01).

REFERENCES

[1] Denry I, Holloway JA. Ceramics for dental applications: a review. Materials 2010;3:351–68, http://dx.doi.org/10.3390/ma3010351.

[2] Piconi C, Maccauro G. Zirconia as a ceramic biomaterial. Biomaterials 1999;20:1–25, http://dx.doi.org/10.1016/S0142-9612(98)00010-6.

[3] Garvie RC, Nicholson PS. Phase analysis in zirconia systems. J Am Ceram Soc 1972;55:303–5, http://dx.doi.org/10.1111/j.1151-2916.1972.tb11290.x.

[4] Garvie RC, Hannink RH, Pascoe RT. Ceramic steel? Nature 1975;258:703, http://dx.doi.org/10.1038/258703a0.

[5] Lawn BR, Pajares A, Zhang Y, Deng Y, Polack MA, Lloyd IK, et al. Materials design in the performance of all-ceramic crowns. Biomaterials 2004;25:2885–92, http://dx.doi.org/10.1016/j.biomaterials.2003.09.050.

[6] NRFA Silva, Bonfante EA, Zavanelli RA, Thompson VP, Ferencz JL, Coelho PG. Reliability of metalloceramic and zirconia-based ceramic crowns. J Dent Res 2010;89:1051–6, http://dx.doi.org/10.1177/0022034510375826.

[7] Zhang Y, Lawn BR. Evaluating dental zirconia. Dent Mater 2019;35:15–23, http://dx.doi.org/10.1016/j.dental.2018.08.291.

[8] Belli R, Monteiro S, Baratieri LN, Katte H, Petschelt A, Lohbauer U. A photoelastic assessment of residual stresses in zirconia-veneer crowns. J Dent Res 2012;91:316–20, http://dx.doi.org/10.1177/0022034511435100.

[9] Saito Y, Tanaka S-I. Residual stress tensor distributions in cracked austenitic stainless steel measured by two-dimensional X-ray diffraction method. Adv Mat Res 2014:996.

[10] Mainjot AK, Schajer GS, Vanheusden AJ, Sadoun MJ. Influence of veneer thickness on residual stress profile in veneering ceramic: measurement by hole-drilling. Dent Mater 2012;28:160–7, http://dx.doi.org/10.1016/j.dental.2011.11.008.

[11] Fardin VP, Bonfante EA, Coelho PG, Janal MN, Tovar N, Witek L, et al. Residual stress of porcelain-fused to zirconia 3-unit fixed dental prostheses measured by nanoindentation. Dent Mater 2018;34:260–71, http://dx.doi.org/10.1016/j.dental.2017.11.013.

[12] Sebastiani M, Massimi F, Merlati G, Bemporad E. Residual micro-stress distributions in heat-pressed ceramic on zirconia and porcelain-fused to metal systems: analysis by FIB–DIC ring-core method and correlation with fracture toughness. Dent Mater 2015;31:1396–405, http://dx.doi.org/10.1016/j.dental.2015.08.158.

[13] Inokoshi M, Yoshihara K, Nagaoka N, Nakanishi M, De Munck J, Minakuchi S, et al. Structural and chemical analysis of the zirconia–Veneering ceramic interface. J Dent Res 2016;95:102–9, http://dx.doi.org/10.1177/0022034515608825.

[14] Lunt AJG, Mohanty G, Ying S, Dluhoš J, Sui T, Neo TK, et al. A comparative transmission electron microscopy, energy dispersive x-ray spectroscopy and spatially resolved micropillar compression study of the yttria partially stabilised zirconia - porcelain interface in dental prosthesis. Thin Solid Films 2015;596:222–32, http://dx.doi.org/10.1016/j.tsf.2015.07.070.

[15] Lunt AJG, Mohanty G, Neo TK, Michler J, Korsunsky AM. Microscale resolution fracture toughness profiling at the zirconia-porcelain interface in dental prostheses. Micro+Nano materials, devices, and systems, vol. 9668. International Society for Optics and Photonics; 2015, http://dx.doi.org/10.1117/12.2199217, 96685S.

[16] Tholey MJ, Berthold C, Swain MV, Thiel N. XRD2 micro-diffraction analysis of the interface between Y-TZP and veneering porcelain: role of application methods. Dent Mater 2010;26:545–52, http://dx.doi.org/10.1016/j.dental.2010.02.002.

[17] Tholey MJ, Swain MV, Thiel N. Thermal gradients and residual stresses in veneered Y-TZP frameworks. Dent Mater 2011;27:1102–10, http://dx.doi.org/10.1016/j.dental.2011.08.001.

[18] Mochales C, Maerten A, Rack A, Cloetens P, Mueller WD, Zaslansky P, et al. Monoclinic phase transformations of zirconia-based dental prostheses, induced by clinically practised surface manipulations. Acta Biomater 2011;7:2994–3002, http://dx.doi.org/10.1016/j.actbio.2011.04.007.
[19] Zhang Y, Lawn BR. Evaluating dental zirconia. Dent Mater 2019;35:15–23, http://dx.doi.org/10.1016/j.dental.2018.08.291.
[20] Zarone F, Russo S, Sorrentino R. From porcelain-fused-to-metal to zirconia: clinical and experimental considerations. Dent Mater 2011;27:83–96, http://dx.doi.org/10.1016/j.dental.2010.10.024.
[21] Denry I, Kelly JR. State of the art of zirconia for dental applications. Dent Mater 2008;24:299–307, http://dx.doi.org/10.1016/j.dental.2007.05.007.
[22] Zenotec Zr Bridge n.d. https://www.ivoclarvivadent.us/explore/zenotec-zr-bridge [Accessed 12 February 2019].
[23] GmbH MAW. Ivoclar Vivadent - IPS e.max Ceram n.d. http://www.ivoclarvivadent.co.uk/en/products/all-ceramics/ips-emax-technicians/ips-emax-ceram (Accessed 12 February 2019).
[24] Chaar MS, Passia N, Kern M. All-ceramic inlay-retained fixed dental prostheses: an update. Quintessence Int 2015;46:781–8, http://dx.doi.org/10.3290/j.qi.a34552.
[25] Belli R, Petschelt A, Lohbauer U. Thermal-induced residual stresses affect the fractographic patterns of zirconia-veneer dental prostheses. J Mech Behav Biomed Mater 2013;21:167–77, http://dx.doi.org/10.1016/j.jmbbm.2012.10.022.
[26] Lunt AJG, Salvati E, Ma L, Dolbyna IP, Neo TK, Korsunsky AM. Full in-plane strain tensor analysis using the microscale ring-core FIB milling and DIC approach. J Mech Phys Solids 2016;C:47–67, http://dx.doi.org/10.1016/j.jmps.2016.03.013.
[27] Korsunsky AM, Sui T, Dluhoš J, Ying S, Lunt AJ, Song B, et al. Multi-beam engineering microscopy-a versatile tool for optimal materials design; 2015.
[28] Lunt AJ, Baimpas N, Salvati E, Dolbnya IP, Sui T, Ying S, et al. A state-of-the-art review of micron-scale spatially resolved residual stress analysis by FIB-DIC ring-core milling and other techniques. J Strain Anal Eng Des 2015;50:426–44, http://dx.doi.org/10.1177/0309324715596700.
[29] Lunt AJG, Korsunsky AM. A review of micro-scale focused ion beam milling and digital image correlation analysis for residual stress evaluation and error estimation. Surf Coat Technol 2015;283:373–88, http://dx.doi.org/10.1016/j.surfcoat.2015.10.049.
[30] Sui T, Lunt AJG, Baimpas N, Sandholzer MA, Li T, Zeng K, et al. Understanding nature's residual strain engineering at the human dentine–enamel junction interface. Acta Biomater 2016;32:256–63, http://dx.doi.org/10.1016/j.actbio.2016.01.009.
[31] Lunt AJG, Chater P, Kleppe A, Baimpas N, Neo TK, Korsunsky AM. Residual strain mapping through pair distribution function analysis of the porcelain veneer within a yttria partially stabilised zirconia dental prosthesis. Dent Mater 2019;35:257–69, http://dx.doi.org/10.1016/j.dental.2018.11.013.
[32] Lunt AJG, Chater P, Korsunsky AM. On the origins of strain inhomogeneity in amorphous materials. Sci Rep 2018;8:1574, http://dx.doi.org/10.1038/s41598-018-19900-2.
[33] Korsunsky AM, Salvati E, Lunt AGJ, Sui T, Mughal MZ, Daniel R, et al. Nanoscale residual stress depth profiling by Focused Ion Beam milling and eigenstrain analysis. Mater Des 2018;145:55–64, http://dx.doi.org/10.1016/j.matdes.2018.02.044.
[34] Korsunsky AM, Sebastiani M, Bemporad E. Focused ion beam ring drilling for residual stress evaluation. Mater Lett 2009;63:1961–3, http://dx.doi.org/10.1016/j.matlet.2009.06.020.
[35] Lunt AJ, Korsunsky AM. Intragranular residual stress evaluation using the semi-destructive FIB-DIC ring-core drilling method. Adv Mat Res 2014:996.
[36] Bemporad E, Brisotto M, Depero LE, Gelfi M, Korsunsky AM, Lunt AJG, et al. A critical comparison between XRD and FIB residual stress measurement techniques in thin films. Thin Solid Films 2014;572:224–31, http://dx.doi.org/10.1016/j.tsf.2014.09.053.
[37] Baimpas N, Lunt AJG, Dolbnya IP, Dluhos J, Korsunsky AM. Nano-scale mapping of lattice strain and orientation inside carbon core SiC fibres by synchrotron X-ray diffraction. Carbon 2014;79:85–92, http://dx.doi.org/10.1016/j.carbon.2014.07.045.
[38] Chai H, JJ-W Lee, Mieleszko AJ, Chu SJ, Zhang Y. On the interfacial fracture of porcelain/zirconia and graded zirconia dental structures. Acta Biomater 2014;10:3756–61, http://dx.doi.org/10.1016/j.actbio.2014.04.016.
[39] Toraya H, Yoshimura M, Somiya S. Calibration curve for quantitative analysis of the monoclinic-tetragonal ZrO2 system by X-ray diffraction. J Am Ceram Soc 1984, 67:C-119-C-121.
[40] Pezzotti G. Raman piezo-spectroscopic analysis of natural and synthetic biomaterials. Anal Bioanal Chem 2005;381:577–90, http://dx.doi.org/10.1007/s00216-004-2780-1.
[41] Clarke IC, Manaka M, Green DD, Williams P, Pezzotti G, Kim Y-H, et al. Current status of zirconia used in total hip implants. JBJS 2003;85:73–84.
[42] Inokoshi M, Shimizu H, Nozaki K, Takagaki T, Yoshihara K, Nagaoka N, et al. Crystallographic and morphological analysis of sandblasted highly translucent dental zirconia. Dent Mater 2018;34:508–18, http://dx.doi.org/10.1016/j.dental.2017.12.008.
[43] Roberts O, Lunt AJ, Ying S, Sui T, Baimpas N, Dolbnya IP, et al. A study of phase transformation at the surface of a zirconia ceramic. Proceedings of the world congress on engineering, vol. 2. Hong Kong: Newswood and International Association of Engineers London; 2014. p. 2–4.
[44] Casellas D, Cumbrera FL, Sánchez-Bajo F, Forsling W, Llanes L, Anglada M. On the transformation toughening of Y–ZrO2 ceramics with mixed Y–TZP/PSZ microstructures. J Eur Ceram Soc 2001;21:765–77, http://dx.doi.org/10.1016/S0955-2219(00)00273-9.
[45] Clarke DR, Adar F. Measurement of the crystallographically transformed zone produced by fracture in ceramics containing tetragonal zirconia. J Am Ceram Soc 1982;65:284–8.
[46] Bradley M. Curve fitting in Raman and IR spectroscopy: basic theory of line shapes and applications. Thermo Fisher Scientific, Madison, USA, Application Note; 2007. p. 50733.
[47] Tamura N, MacDowell AA, Spolenak R, Valek BC, Bravman JC, Brown WL, et al. Scanning X-ray microdiffraction with submicrometer white beam for strain/stress and orientation mapping in thin films. J Synchrotron Radiat 2003;10: 137–43.
[48] Tamura N, MacDowell AA, Celestre RS, Padmore HA, Valek B, Bravman JC, et al. High spatial resolution grain orientation and strain mapping in thin films using polychromatic submicron x-ray diffraction. Appl Phys Lett 2002;80:3724–6.
[49] Lunt AJG, Xie MY, Baimpas N, Zhang SY, Kabra S, Kelleher J, et al. Calculations of single crystal elastic constants for yttria partially stabilised zirconia from powder diffraction data. J Appl Phys 2014;116, http://dx.doi.org/10.1063/1.4891714, 053509.
[50] Eberl C. Digital Image Correlation and Tracking - File Exchange - MATLAB Central n.d. https://uk.mathworks.com/

matlabcentral/fileexchange/12413 [Accessed 12 February 2019].
[51] Korsunsky AM, Sebastiani M, Bemporad E. Residual stress evaluation at the micrometer scale: analysis of thin coatings by FIB milling and digital image correlation. Surf Coat Technol 2010;205:2393–403, http://dx.doi.org/10.1016/j.surfcoat.2010.09.033.
[52] Salvati E, Lunt AJ, Sui T, Korsunsky AM. An investigation of residual stress gradient effects in FIB-DIC micro-ring-Core analysis. Proceedings of the International MultiConference of Engineers and Computer Scientists 2015, 2.
[53] Salvati E, Sui T, Ying S, Lunt AJ, Korsunsky AM. On the accuracy of residual stress evaluation from Focused Ion Beam DIC (FIB-DIC) ring-core milling experiments n.d.
[54] Salvati E, Sui T, Lunt AJG, Korsunsky AM. The effect of eigenstrain induced by ion beam damage on the apparent strain relief in FIB-DIC residual stress evaluation. Mater Des 2016;92:649–58, http://dx.doi.org/10.1016/j.matdes.2015.12.015.
[55] Salvati E, Lunt AJG, Ying S, Sui T, Zhang HJ, Heason C, et al. Eigenstrain reconstruction of residual strains in an additively manufactured and shot peened nickel superalloy compressor blade. Comput Methods Appl Mech Eng 2017;320:335–51, http://dx.doi.org/10.1016/j.cma.2017.03.005.
[56] Müller WH, Pezzotti G. Micromechanics of fracture in partially stabilized zirconia (PSZ) studiedby in-situ Raman spectroscopy. PAMM: proceedings in applied mathematics and mechanics, vol. 5. Wiley Online Library; 2005. p. 349–50.
[57] Wu X, Yu J, Ren T, Liu L. Micro-Raman spectroscopy measurement of stress in silicon. Microelectronics J 2007;38:87–90, http://dx.doi.org/10.1016/j.mejo.2006.09.007.
[58] Lambropoulos JC. Shear, shape and orientation effects in transformation toughening. Int J Solids Struct 1986;22:1083–106.
[59] Scherrer SS, Mekki M, Crottaz C, Gahlert M, Romelli E, Marger L, et al. Translational research on clinically failed zirconia implants. Dent Mater 2019;35:368–88, http://dx.doi.org/10.1016/j.dental.2018.11.033.
[60] Ibegazene H, Alperine S, Diot C. Microstructure of yttria stabilized zirconia-hafnia plasma sprayed thermal barrier coatings. Le Journal de Physique IV 1993;3. C7-1013-C7-1016.
[61] Lelait L, Alperine S. TEM investigations of high toughness non-equilibrium phases in the ZrO 2-Y 2 O 3 system. Scr Metall Mater 1991;25:1815–20.
[62] Eischen JW, Chung C, Kim JH. Realistic modeling of edge effect stresses in bimaterial elements. J Electron Packag 1990;112:16–23, http://dx.doi.org/10.1115/1.2904333.
[63] Aydiner CC, Ü:Ustü:Undag E, Hanan JC. Thermal-tempering analysis of bulk metallic glass plates using an instant-freezing model. Metall Mater Trans A 2001;32:2709–15, http://dx.doi.org/10.1007/s11661-001-1023-8.
[64] Chevalier J, Gremillard L, Virkar AV, Clarke DR. The tetragonal-monoclinic transformation in zirconia: lessons learned and future trends. J Am Ceram Soc 2009;92:1901–20.
[65] Durand J-C, Jacquot B, Salehi H, Fages M, Margerit J, Cuisinier FJG. Confocal Raman microscopic analysis of the zirconia/feldspathic ceramic interface. Dent Mater 2012;28:661–71, http://dx.doi.org/10.1016/j.dental.2012.02.013.
[66] Lughi V, Sergo V. Low temperature degradation -aging- of zirconia: a critical review of the relevant aspects in dentistry. Dent Mater 2010;26:807–20, http://dx.doi.org/10.1016/j.dental.2010.04.006.
[67] Kohorst P, Borchers L, Strempel J, Stiesch M, Hassel T, Bach F-W, et al. Low-temperature degradation of different zirconia ceramics for dental applications. Acta Biomater 2012;8:1213–20, http://dx.doi.org/10.1016/j.actbio.2011.11.016.
[68] Cattani-Lorente M, Scherrer SS, Ammann P, Jobin M, Wiskott HWA. Low temperature degradation of a Y-TZP dental ceramic. Acta Biomater 2011;7:858–65, http://dx.doi.org/10.1016/j.actbio.2010.09.020.
[69] Gupta TK, Bechtold JH, Kuznicki RC, Cadoff LH, Rossing BR. Stabilization of tetragonal phase in polycrystalline zirconia. J Mater Sci 1977;12:2421–6.
[70] Charalambides PG, McMeeking RM. Near-tip mechanics of stress-induced microcracking in brittle materials. J Am Ceram Soc 1988;71:465–72.
[71] Gupta TK, Lange FF, Bechtold JH. Effect of stress-induced phase transformation on the properties of polycrystalline zirconia containing metastable tetragonal phase. J Mater Sci 1978;13:1464–70.
[72] Zhang P, Li SX, Zhang ZF. General relationship between strength and hardness. Mater Sci Eng A 2011;529:62–73, http://dx.doi.org/10.1016/j.msea.2011.08.061.
[73] Baldassarri M, Stappert CFJ, Wolff MS, Thompson VP, Zhang Y. Residual stresses in porcelain-veneered zirconia prostheses. Dent Mater 2012;28:873–9, http://dx.doi.org/10.1016/j.dental.2012.04.019.
[74] Kler MD, Jager ND, Meegdes M, JMVD Zel. Influence of thermal expansion mismatch and fatigue loading on phase changes in porcelain veneered Y-TZP zirconia discs. J Oral Rehabil 2007;34:841–7, http://dx.doi.org/10.1111/j.1365-2842.2006.01675.x.
[75] Yang F, Zhao X, Xiao P. In situ measurement of stresses and phase compositions of the zirconia scale during oxidation of zirconium by Raman spectroscopy. Oxid Met 2014;81:331–43, http://dx.doi.org/10.1007/s11085-013-9433-8.
[76] Nielsen JP, Tuccillo JJ. Calculation of interfacial stress in dental porcelain bonded to gold alloy substrate. J Dent Res 1972;51:1043–7.
[77] Swain MV. Shape memory behaviour in partially stabilized zirconia ceramics. Nature 1986;322:234, http://dx.doi.org/10.1038/322234a0.
[78] Asaoka K, Kuwayama N, Tesk JA. Influence of tempering method on residual stress in dental porcelain. J Dent Res 1992;71:1623–7.
[79] Reginato VF, Kemmoku DT, Caldas RA, Bacchi A, Pfeifer CS, Consani RLX, et al. Characterization of residual stresses in veneering ceramics for prostheses with zirconia framework. Braz Dent J 2018;29:347–53, http://dx.doi.org/10.1590/0103-6440201801990.
[80] Zhang Y, Allahkarami M, Hanan JC. Measuring residual stress in ceramic zirconia–porcelain dental crowns by nanoindentation. J Mech Behav Biomed Mater 2012;6:120–7, http://dx.doi.org/10.1016/j.jmbbm.2011.11.006.
[81] Al-Amleh B, Neil Waddell J, Lyons K, Swain MV. Influence of veneering porcelain thickness and cooling rate on residual stresses in zirconia molar crowns. Dent Mater 2014;30:271–80, http://dx.doi.org/10.1016/j.dental.2013.11.011.
[82] Trunec M, Chlup Z. Higher fracture toughness of tetragonal zirconia ceramics through nanocrystalline structure. Scr Mater 2009;61:56–9, http://dx.doi.org/10.1016/j.scriptamat.2009.03.019.
[83] Lunt AJG, Kabra S, Kelleher J, Zhang SY, Neo TK, Korsunsky AM. Tensile secondary creep rate analysis of a dental veneering porcelain. Thin Solid Films 2015;596:269–76, http://dx.doi.org/10.1016/j.tsf.2015.05.039.
[84] Lunt A, Terry A, Ying S, Baimpas N, Sui T, Kabra S, et al. Characterisation of nanovoiding in dental porcelain using small angle neutron scattering and transmission electron microscopy. Dent Mater 2017;33:486–97, http://dx.doi.org/10.1016/j.dental.2017.02.005.

[85] Lofaj F, Okada A, Usami H, Kawamoto H. Creep damage in an advanced self-reinforced silicon nitride: part I, cavitation in the amorphous boundary phase. J Am Ceram Soc 1999;82:1009–19.

[86] Mainjot AK, Schajer GS, Vanheusden AJ, Sadoun MJ. Influence of zirconia framework thickness on residual stress profile in veneering ceramic: measurement by hole-drilling. Dent Mater 2012;28:378–84, http://dx.doi.org/10.1016/j.dental.2011.11.009.

[87] Technical IV. IPS e.max Ceram - Instructions for use; 2019 https://www.ivoclarvivadent.com/zoolu-website/media/document/1264/IPS+e-max+Ceram.

[88] Lunt AJ, Neo TK, Korsunsky AM. An electron microscopy study of sintering in three dental porcelains; 2015.

[89] Scherrer SS, Robert Kelly J, Quinn GD, Xu K. Fracture toughness (KIc) of a dental porcelain determined by fractographic analysis. Dent Mater 1999;15:342–8, http://dx.doi.org/10.1016/S0109-5641(99)00055-X.

[90] Schmitt J, Holst S, Wichmann M, Reich S, Göllner M, Hamel J. Zirconia posterior fixed partial dentures: a prospective clinical 3-year follow-up. Int J Prosthodont 2009;22: 597.

[91] Guazzato M, Walton TR, Franklin W, Davis G, Bohl C, Klineberg I. Influence of thickness and cooling rate on development of spontaneous cracks in porcelain/zirconia structures. Aust Dent J 2010;55:306–10, http://dx.doi.org/10.1111/j.1834-7819.2010.01239.x.

[92] Isgrò G, Kleverlaan CJ, Wang H, Feilzer AJ. The influence of multiple firing on thermal contraction of ceramic materials used for the fabrication of layered all-ceramic dental restorations. Dent Mater 2005;21:557–64, http://dx.doi.org/10.1016/j.dental.2004.08.006.

[93] Wolfart M, Lehmann F, Wolfart S, Kern M. Durability of the resin bond strength to zirconia ceramic after using different surface conditioning methods. Dent Mater 2007;23:45–50, http://dx.doi.org/10.1016/j.dental.2005.11.040.

[94] Saito A, Komine F, Blatz MB, Matsumura H. A comparison of bond strength of layered veneering porcelains to zirconia and metal. J Prosthet Dent 2010;104:247–57, http://dx.doi.org/10.1016/S0022-3913(10)60133-3.

[95] Komine F, Saito A, Kobayashi K, Koizuka M, Koizumi H, Matsumura H. Effect of cooling rate on shear bond strength of veneering porcelain to a zirconia ceramic material. J Oral Sci 2010;52:647–52, http://dx.doi.org/10.2334/josnusd.52.647.